Synthesis And Magnetic Properties Of Spherical Maghemite Nanoparticles With Tunable Size And Surface Chemistry

Sakina Meftah, Anh-Tu Ngo, Laurent Bouteiller, Vincent Russier, David Hrabovsky, Adama Konaté, Djimédo Kondo, Fahmi Bedoui, Isabelle Lisiecki

SYNTHESIS AND MAGNETIC PROPERTIES OF SPHERICAL MAGHEMITE NANOPARTICLES WITH TUNABLE SIZE AND SURFACE CHEMISTRY.

Sakina Meftah[1,2], Anh-Tu Ngo[1], Laurent Bouteiller[3], Vincent Russier[4], David Hrabovsky[5], Adama Konaté[6], Djimédo Kondo[7], Fahmi Bedoui[2,8] Isabelle Lisiecki[1*]

1- Sorbonne Université, CNRS, De la Molécule aux Nano-Objets: Réactivité, Interactions Spectroscopies, MONARIS, 75005 Paris, France
2- Université de technologie de Compiègne, Roberval (Mechanics, energy and electricity), Centre de recherche Royallieu - CS 60 319 - 60 203 Compiègne Cedex.
3- Sorbonne Université, CNRS, Institut Parisien de Chimie Moléculaire, IPCM, 75005 Paris, France
4- ICMPE UMR 7182 CNRS and Université UPE, 2-8 rue Henri Dunant, 94320 Thiais, France.
5- Plateforme Mesures Physiques à Basses Températures (MPBT), Sorbonne Université, 75005 Paris, France
6- Service d'Analyse Physico-Chimique, Université de Technologie de Compiègne, BP 20529, Compiègne Cedex F-60205, France
7- Sorbonne Université, CNRS, Institut Jean Le Rond D'Alembert, 75005 Paris, France
8- California institute of Technology, Materials and Process simulation Center, 91106, Pasadena, CA, USA

KEYWORDS: Thermal decomposition approach, maghemite nanoparticles, size control, surface chemistry control, magnetic properties.

ABSTRACT: We report the synthesis of uniform populations of spherical maghemite nanoparticles by thermal decomposition of iron precursors, with tunable diameters centered at 3.3, 7.5, and 12.0 nm and tunable surface chemistry. The three stabilizing ligands were fatty acids with three different alkyl chain lengths (18, 12, and 8 carbon atoms). The unprecedented accurate control of the surface chemistry is made possible by the use of three types of iron complexes, that is, iron oleate (C18), iron dodecanoate (C12), and iron octanoate (C8), associated with fatty acid ligands having the same alkyl chain length, that is, oleic acid (C18), dodecanoic acid (C12), and octanoic acid (C8). Since the thermal decomposition of the iron precursor varies with the chain length, no general rules can be applied to control the nanoparticle size, but optimal synthesis conditions have been investigated to induce the growth of nanoparticles with three different surface chemistries, keeping the diameters centered at 3.3, 7.5, and 12.0 nm. Finally, structural characterization of the nine populations of maghemite nanoparticles was performed by transmission electron microscopy and X-ray diffraction, and magnetic properties were determined using SQUID magnetometry.

1. INTRODUCTION

Over the past two decades, the synthesis of iron oxide nanoparticles (NPs) has seen significant advance, driven by their potential in a wide range of technological applications, including data recording[1], catalysis[2], wastewater treatment[3], and biomedicine[4].

Among these iron oxides, magnetite (Fe_3O_4) has been prominently featured in literature, particularly for its use in magnetic resonance imaging (MRI) and magnetic hyperthermia due to its high saturation magnetization. However, maghemite (γ-Fe_2O_3), a closely related iron oxide, exhibits distinct properties. Unlike magnetite, maghemite is fully oxidized, and contains only Fe^{3+} ions, which provides superior chemical stability. This increased stability is valuable for applications requiring long-term performance, such as environmental remediation and drug delivery[5]. Furthermore, the surface chemistry of maghemite is more conducive to uniform functionalization, thereby improving its effectiveness. In addition, the absence of Fe^{2+} ions in maghemite results in lower toxicity, making it a safer choice for biomedical applications[6]. These unique properties of maghemite underscore its importance in advancing the capabilities of iron oxide nanoparticles across various fields.

Further accurate control of their structural and chemical characteristics (size, shape/geometry, nanocrystallinity, composition, and surface chemistry) is fundamental for continuously improving their performance. Among the numerous chemical routes developed to produce iron oxide NPs[7], the thermal decomposition of organometallic precursors is the most suitable for inducing NPs with low polydispersity. However, many key parameters must be controlled to successfully prepare well-defined populations of iron-oxide NPs with tunable size[8–15] and shape[3,16–24]. These key parameters include the reaction parameters (heating rate, reaction time, and reaction temperature), the nature of the reagents (precursors, stabilizing surfactant, solvent), the concentration of reagents, the surfactant-to-precursor ratio, and the possible presence of additives[25,26]. The purity of the reagents is another key parameter for the reproducibility of these syntheses. For example, it has been shown that commercial iron precursors have been successfully used for several years to form spherical maghemite NPs, while the “same” purchased precursor now yields anisotropic-shaped NPs because of the presence of impurities that strongly affect particle growth[27].

The complexity of these syntheses is not only due to the full set of involved parameters but also to the intricate interplay between these parameters. For instance, there are still controversies in the literature regarding the effect of the ligand/precursor ratio, which, according to different studies can promote an increase or decrease in the final size[28]. When one parameter differs from one synthesis to another, this may impact the role played by others, avoiding, in this case, the establishment of general rules concerning the nucleation and growth processes of the NPs.

This can explain why the synthesis of maghemite NPs coated with tunable carboxylic acid chain lengths through the thermal decomposition of iron carboxylic acid complexes, keeping their size unchanged, has never been reported. Indeed, in this case, varying the nature of the coating ligands surrounding the particles implies a change similar to that of the precursor and that of the stabilizing ligand, which can drastically impact the nucleation and/or growth process and, in turn, the NP size and/or shape. Most of the time, only the nature of the ligand is changed while keeping the iron precursor unchanged, which results in the mixing of the two ligands, taking part in the passivation of the NPs[14].

From a fundamental point of view, controlling the surface chemistry of the NPs is crucial. On the one hand, this allows for the control of interactions between NPs during the growth of their 2D and 3D assemblies. Hence, the alkyl chain length has been shown to dictate the crystalline structure[29,30], interparticle distance[31], and coherence length[32] in plasmonic NPs supercrystal, allowing fine control of their physical properties. On the other hand, when the coated NPs are incorporated in a soft matrix (e.g., a polymer), the ligand plays a paramount role in achieving optimal dispersion as well as in the properties of the matrix, which can be influenced by the interaction ligand/matrix[33,34]. Whether NPs interact with each other in supercrystals or in a specific environment to form nanocomposites, accurate control of both size and surface chemistry is crucial.

This paper reports the synthesis of spherical maghemite NPs of three different sizes, centered at 3.3, 7.5, and 12.0 nm, and three different coating agents characterized by different alkyl chain lengths (18, 12 and 8 carbons). An unprecedented series of nine NP populations were obtained by investigating the

thermal decomposition of three iron complexes, that is, iron oleate (C18), iron dodecanoate (C12), and iron octanoate (C8), in the presence of stabilizing ligands with the same alkyl chain length, that is, oleic acid (C18), dodecanoic acid (C12), and octanoic acid (C8).
The structural characterization performed by transmission electron microscopy, X-ray diffraction, and magnetic properties performed by SQUID magnetometry of the nine populations of maghemite NPs are presented.

2. EXPERIMENTAL SECTION

2.1. Chemical products

All the materials were used as purchased without further purification. Iron (III) chloride ($FeCl_3.6H_2O$, 99%, VWR), Sodium Oleate (>97.0%, TCI), sodium dodecanoate (>97 %, TCI), sodium n-Octanoate (>99 %, TCI), 1-Hexadecene (for synthesis, Sigma-Aldrich), 1-Octadecene (technical grade, 90 %, Sigma-Aldrich), oleic acid (technical grade, 90 %, Sigma-Aldrich), dodecanoic acid (99 %, Thermo Scientific), and octanoic acid (99 %, Thermo Scientific) were used.

2.2. Synthesis of iron(X)$_3$ precursors (X = oleate, dodecanoate, octanoate)

Three iron$(X)_3$ precursors (*X = oleate, dodecanoate, and octanoate*) were prepared by the reaction of iron (III) chloride salt ($FeCl_3$) with the corresponding sodium fatty acid salts, sodium oleate, sodium dodecanoate, and sodium octanoate. The synthesis of the iron $(oleate)_3$ precursor was based on a method reported by Park *et al.*.[11]. Iron chloride (10.8 g, 40 mmol) and sodium oleate 36.5 g (120 mmol) were solubilized in a mixture of solvents composed of 80 ml of ethanol, 60 ml of distilled water, and 140 ml of hexane. The reaction mixture was heated to 70 °C and maintained at that temperature for 4 h until the reaction was complete. The upper phase containing the iron-oleate complex was then collected using a separating funnel and subjected to three washing steps with 30 ml of distilled water. Subsequently, hexane was evaporated using a rotary evaporator, yielding an iron-oleate complex in a waxy red-brown paste form. A similar method was used to prepare iron$(dodecanoate)_3$ and iron$(octanoate)_3$ by replacing sodium oleate with sodium dodecanoate and octanoate, respectively.

2.3. Transmission Electron Microscopy (TEM)

Transmission Electron Microscopy (TEM) was performed using a JEOL JEM-1011 microscope operated at 100 kV. For the TEM analysis, drops of the colloidal solution were deposited onto an amorphous carbon-coated TEM grid. The average diameter and polydispersity of the nanoparticles (NPs) were determined by measuring the diameters of over 700 NPs from the TEM images using the ImageJ software. The mean diameter was calculated as the average of these measurements, and polydispersity was assessed based on the standard deviation relative to the mean size.

2.4. X-ray diffraction

X-ray diffraction of the nanoparticles was carried out using a Bruker D8 Advance X-ray diffractometer provided by the Service Analyses Physico-Chimiques (SAPC) at the Université de Technologie de Compiègne. The instrument was operated at 30 kV and 40 mA, with an X-ray wavelength of 0.1506 nm. The scanning encompassed a 2θ range of 25°-70°, with increments of 0.02°. All the nanoparticle samples were in powder form. For the analysis, the samples were deposited on a holder with a silicon monocrystal.

2.5. Elemental analysis

The chemical compositions of the iron precursors were determined using energy dispersive X-ray spectrometry (EDS) analysis, conducted on a scanning electron microscope (SEM, Quanta FEG 250, Thermo Fisher) equipped with Quantax – X-Flash (Synergie4 – Bruker). This analysis was performed at the Service Analyses Physico-Chimiques (SAPC) at the Université de Technologie de Compiègne.

2.6. Differential scanning calorimetry (DSC)

DSC analysis was performed to investigate the thermal properties of iron $(oleate)_3$, iron $(dodecanoate)_3$, and iron $(octanoate)_3$. The analysis was performed using a DSC Q200 instrument with version 24.11 Build 124 software. DSC thermograms were obtained in the temperature range of [25–400 °C] at a heating rate of 10 °C/min. For sample preparation, approximately 1.3 mg of the product was used, and measurements were conducted with a Tzero Aluminum Hermetic pan under a nitrogen atmosphere.

2.7. Magnetic measurements

Magnetic measurements were carried out on a commercial superconducting quantum interference device (SQUID) magnetometer (MPMS3, Quantum Design, USA) with a field of 1.59×10^3 Am^{-1} for the zero-field-cooled (ZFC)/field-cooled (FC) susceptibility curves and with fields up to 3.98×10^6 Am^{-1} for the magnetization curves. All magnetic measurements were performed on a film of powdered iron oxide NPs. During the measurement, the applied field was parallel to the iron-oxide NP film. For the ZFC measurements, the sample was cooled from 300 to 3 K with no field and then heated to 300 K in a field of 1.59×10^3 Am^{-1} to record the magnetization $M_{ZFC}(T)$ of the sample. For the FC measurements, the sample was cooled again to 3 K under the same applied field, and the magnetization M_{FC} (T) was recorded. In both cases, the measurements were performed on heating with a heating rate on the order of 2 K min^{-1} for each temperature step. The measurement time was ~ 5 s. The hysteresis curves were obtained at 3 K.

3. RESULTS AND DISCUSSION

To synthesize spherical maghemite NPs with three different diameters, centered at 3.3, 7.5, and 12.0 nm, and stabilized with three different carboxylic acid chain lengths, we adapted the procedure reported by Park et al., which involves the thermal decomposition of iron oleate in the presence of oleic acid (C18)[11], giving rise to oleic acid-coated maghemite NPs. The unprecedented accurate *control of the NP surface chemistry* we present here was obtained thanks to the use of three types of precursors, iron oleate, iron dodecanoate, and iron octanoate complexes, associated with their corresponding carboxylic acids, that is, oleic acid (C18), dodecanoic acid (C12), and octanoic acid (C8). For the three types of surface chemistry, that is, by using the three associated types of precursors, the *control of the NP size* is obtained by using various strategies including the well-known solvent effect[11]. Indeed, it is now well established that the higher the boiling point of the solvent, for instance, tetradecene (251°C), hexadecene (274°C), or octadecene (318 °C), the larger the NPs. However, this strategy is somewhat limited, particularly for the synthesis of smaller NPs (~ 3 nm) (*see below*). In addition, the thermal decomposition of the three precursors was strongly dependent on the carboxylic acid chain length. This means that the nucleation and growth processes differ from one precursor to another, which in turn requires the adaptation of the synthesis conditions from one precursor to another. Therefore, the size control of maghemite NPs stabilized with C18, C12, and C8 ligands involves not only the solvent effect strategy but also other ones, adapted to the different types of precursors. For convenience, NPs with a mean diameter centered at 3.3, 7.5, and 12.0 nm are named small, intermediate, and large-size NPs, respectively.

The dependence of the thermal decomposition of the precursors with the carboxylic acid chain length is illustrated by a differential scanning calorimetry (DSC) analysis. TEM and X-ray diffraction studies were performed to characterize the structural parameters of the nine populations of maghemite NPs with diameters centered at 3.3, 7.5, and 12.0 nm and stabilized with C18, C12, and C8 carboxylic acids. The magnetic properties of the nine populations were investigated.

3.1. Thermal decomposition study of the iron precursors by differential scanning calorimetry (DSC)

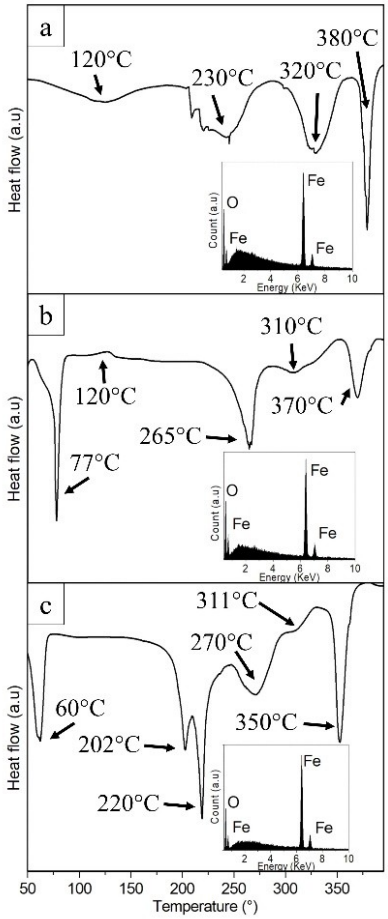

Figure 1. Differential scanning calorimetry (DSC) of the (a) iron oleate, (b) iron dodecanoate, and (c) iron octanoate precursors. Insets: corresponding energy dispersive X-ray spectrometry (EDS) patterns.

The thermal decomposition of the precursors, iron oleate (C18), iron dodecanoate (C12), and iron octanoate (C8), was analyzed using differential scanning calorimetry (DSC) to elucidate the differences in their decomposition behavior as influenced by the carboxylic acid chain length. DSC was chosen for its ability to precisely capture the enthalpic changes associated with the decomposition process, thereby providing detailed insight into the distinct thermal characteristics of each precursor[11,35]. The results are shown in Figure 1.

The DSC pattern of iron oleate (C18) (Figure 1a) showed a weak endothermic peak at 120 °C, which can be attributed to the removal of crystal hydrate water. In good agreement with previous studies[11,35,36], an endothermic peak was observed at 230 °C, which corresponds to the dissociation of the first oleate group from the precursor, whereas the next peak, at 320 °C, was assigned to the dissociation of the two remaining ligands. The former was associated with the nucleation step, whereas the latter was associated with the growth step. At higher temperatures (approximately 380 °C), the last peak corresponds to the complete decomposition of the precursor.
The DSC pattern of the iron dodecanoate (C12) precursor (Figure 1b) showed low-temperature peaks at approximately 77 °C. Elemental analysis revealed that only iron was present. The absence of other elements such as chlorine or sodium reveals the absence of impurities such as sodium dodecanoate, which could result either from nonstoichiometric conditions during their synthesis or from a non-optimal washing step[27]. The peak obtained at low temperatures can only be assigned to the melting point of this precursor, which is solid at room temperature, unlike iron oleate (C18). Two endothermic peaks were observed at 265 °C and 310 °C. Because of the similar behavior observed for iron oleate, it

can be assumed that these two endothermic peaks correspond to the nucleation and growth peaks, respectively. However, the nucleation peak was found at higher temperatures compared to that of the oleic precursor (265 °C versus 230 °C). This indicates that the nucleation step requires a significantly higher temperature for the dodecanoate precursor than for the oleic precursor. The second endothermic peak at 310 °C occurred at a slightly lower temperature than that of the oleic precursor. Comparative measurements of the DSC patterns of oleic and dodecanoic precursors show that the effective separation of the nucleation and growth processes taking place at different temperatures is less in the latter than in the former. Complete decomposition occurs at approximately 370 °C, which is lower than that of the oleic precursor.

Focusing on the iron octanoate (C8) precursor (Figure 1c), a low-temperature peak is observed at 60°C. As for the precursor iron dodecanoate (C12), this peak could be attributed to its melting point. However, unlike the behavior observed for the C18 and C12 precursors, which displayed two peaks attributed to the nucleation and growth steps, three peaks at 202, 220, and 270 °C were obtained for the C8 precursor. It is possible that each of these three peaks corresponds to the dissociation of an octanoate group from the precursor; however, in any case, they reveal a more complex dissociation pathway than in the case of C18 and C12 precursors. Finally, complete decomposition occurs at approximately 350 °C, which is lower than the temperatures of the oleic and dodecanoic precursors.

3.2. Transmission electron microscopy (TEM) study

3.2.1. Size control of oleic acid (C18)-coated maghemite nanoparticles

The synthesis of larger oleic acid (C18)-coated maghemite NPs was based on the procedure reported by Park and Co.[11]. 1.42 g (1.6 mmol) of the iron oleate precursor and 0.22 g (0.8 mmol) of oleic acid were dissolved in 10 ml of octadecene. The precursor-to-ligand concentration ratio R was equal to 2. This mixture was heated to the boiling point of octadecene (318 °C), refluxed for 30 min, and cooled to room temperature (Table 1). A black solution was formed, which was washed with a large excess of acetone, followed by centrifugation at 4900 rpm for 10 min. Oleic acid-coated NPs were dispersed in chloroform. Figure 2a shows the TEM image of the resulting C18-NPs, revealing a population composed of highly uniform spherical NPs, with a mean diameter and a size polydispersity of 12.6 nm and 4 %, respectively (Inset of Figure 2a).

Using a lower boiling point (bp) solvent, hexadecene (bp: 274 °C), other things being equal, the mean diameter decreases from 12.6 nm to 7.8 nm, keeping a low size polydispersity of 4 % (Figure 2b and Inset of Fig 2b). This behavior is explained by the lower growth activation resulting from the use of a solvent, whose boiling point (274 °C) is lower than the growth peak (300 °C), (Figure 1) compared to the octadecene (318 °C)[11,12,14,16].

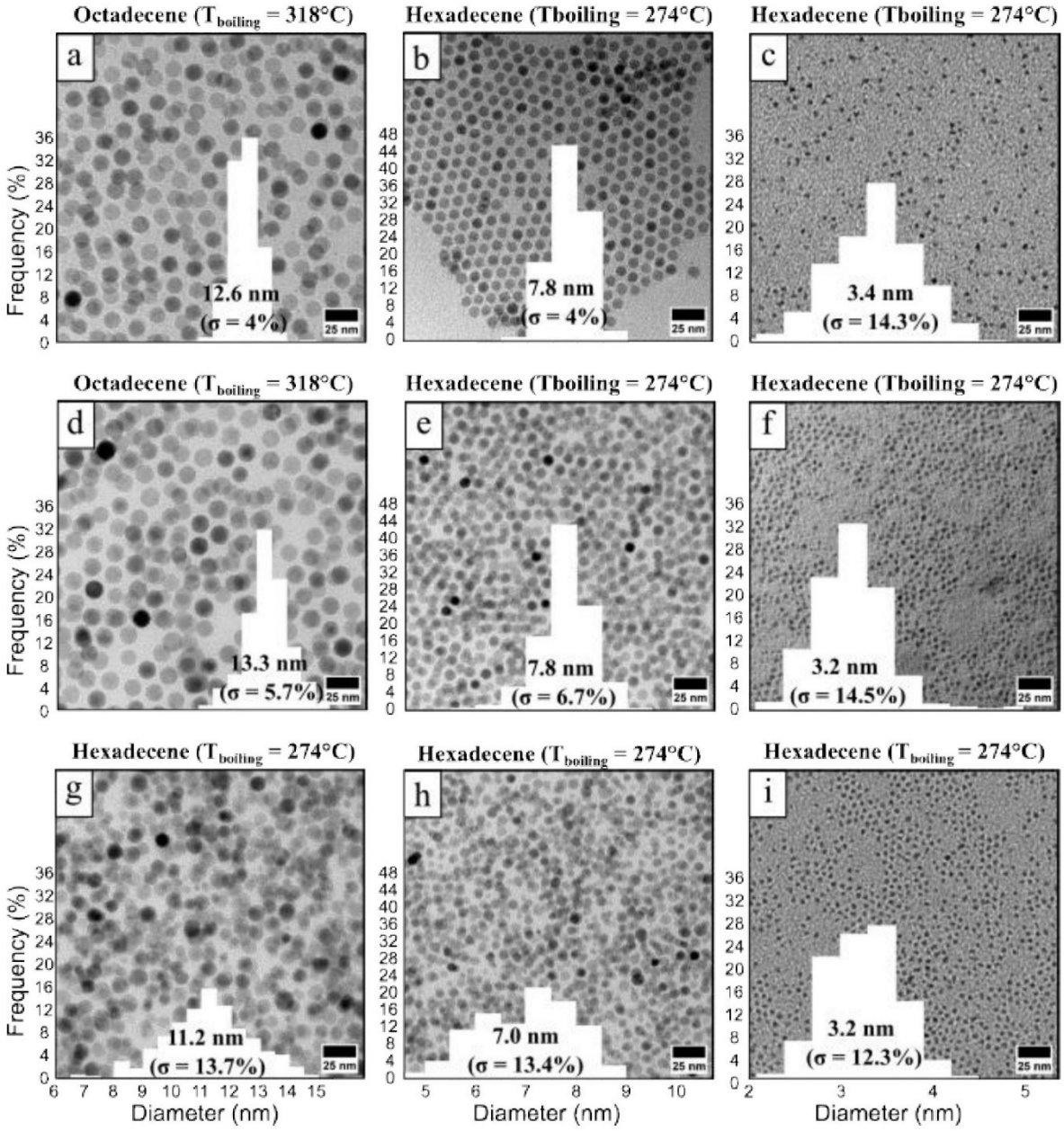

Figure 2. Transmission electron microscopy (TEM) images of maghemite nanoparticles synthesized from (a,b,c) iron oleate, (d,e,f) iron dodeconaoate, and (g,h,i) iron octanoate. The mean diameters are centered on (a,d,g) 12.0 nm, (b,e,g) 7.5 nm and (c,f,i) 3.3 nm.

The very low NP-size polydispersity (4 % for both cases) is explained by the specific separation of the nucleation and growth processes. Indeed, the DSC measurement shows a nucleation peak at approximately 230 °C, corresponding to the first oleate ligand dissociation from the iron oleate, while at approximately 320 °C, the remaining two oleate ligands dissociate in their turns, inducing NP growth (Figure 1a).

By further decreasing the reaction temperature through the use of tetradecene (251 °C), other things being equal, a population of small NPs (~ 2.6 nm) was obtained; however, a very low reaction yield and high size polydispersity (20 %) were observed. This behavior is attributed to the fact that the reaction temperature is close to the nucleation peak, thus hindering the decomposition of all precursors. The solvent strategy, through the use of tetradecene, being unsuccessful in producing the smaller NPs, we kept the procedure giving the 7.8 nm C18-NPs with the following modifications: the

precursor concentration is increased from 1.6 mmol to 4 mmol, keeping unchanged the ratio R equal to 2, as well as the solvent, hexadecene and the reflux time, 30 min (Table 1). As shown in (Figure 2c), these conditions led to the formation of 3.4 nm with a size polydispersity of 14.3 %. The decrease in the mean NP size with increasing precursor concentration results from the enhancement of iron supersaturation before nucleation and is explained by the LaMer supersaturation theory[37,38].

Table 1. Parameters used for the synthesis of maghemite nanoparticles by thermal decomposition approach with the TEM size measured.

	Precursor (mmol)	***Ligand (mmol)***	***R=[P/L]***	***Solvent (T_{bp} °C)***	***Reflux Time (min)***	***TEM Diameter (nm)***
C18-NPs	1.6	0.8	2.0	Octadecene (318°C)	30	12.6 (σ = 4%)
	1.6	0.8	2.0	Hexadecene (274°C)	30	7.8 (σ = 4%)
	4.0	2.0	2.0	Hexadecene (274°C)	30	3.4 (σ = 14.3%)
C12-NPs	1.6	3.2	0.50	Octadecene (318°C)	30	13.3 (σ = 5.7%)
	0.8	1.6	0.50	Hexadecene (274°C)	60	7.8 (σ = 6.7%)
	0.8	2.8	0.29	Hexadecene (274°C)	60	3.2 (σ = 14.5%)
C8-NPs	1.6	2.0	0.80	Hexadecene (274°C)	90	11.2 (σ = 13.7%)
	1.6	2.0	0.80	Hexadecene (274°C)	60	7.0 (σ = 13.4%)
	3.2	6.3	0.50	Hexadecene (274°C)	30	3.2 (σ = 12.3%)

3.2.2. Size control of dodecanoic acid (C12)-coated maghemite nanoparticles

By repeating the procedure used to obtain the larger C18-NPs (see &3.2.1), with iron dodecanoate as a precursor instead of iron oleate, we obtained polydisperse C12-NPs (σ = 17 %) with a mean diameter of 14.0 nm instead of low polydisperse 12.6 nm NPs. As before, the change in the quality of the populations can be explained by the change in the decomposition processes of the two iron precursors. For iron oleate, the nucleation and growth peaks are at around 230 °C and 320 °C, respectively compared to 265 °C and 310 °C for iron dodecanoate (Figure 1). To overcome the variation of the nucleation and growth kinetics from the iron oleate to the iron dodecanoate, and then successfully obtain uniform C12-NPs with a mean diameter centered on 12 nm, the precursor and ligand concentrations have been modified as follows: 1.045 g (1.6 mmol) of iron dodecanoate precursor and 0.64 g (3.2 mmol) of dodecanoic acid have been used, giving a ratio, R, of 0.5. The solvent used remained unchanged, that is, octadecene (318 °C), as well as the reflux time 30 min (Table 1). Under optimized conditions, the TEM image and size histogram (Figure 2d and inset of Figure 2d) illustrate the formation of 13.3 nm C12-NPs with a low polydispersity of 5.7 %.

Similar to the synthesis of the intermediate C18-NP size, we used a lower-boiling solvent, hexadecene, instead of octadecene to form the intermediate C12-NP size. The resulting C12-NPs were highly polydispersed (16 %) with a mean diameter of 6.3 nm. By adjusting the conditions, i.e., by decreasing the precursor concentration from 1.6 mmol to 0.8 mmol, keeping unchanged the ratio R, and increasing the reflux time from 30 min to 60 min, low-size polydispersity C12-NPs (6.7 %) with a mean diameter of 7. 8 nm were obtained (Figure 2e and the Inset of Figure 2e). This behavior illustrates the importance of the nature of the Fe precursor.

By adjusting the ratio, R, to 0.28 (instead of 0.5 for the 7.8 nm C12-NPs), that is, by increasing the dodecanoic acid ligand concentration, other things being equal, 3.2 nm C12-NPs with a size polydispersity of 14.5 % were obtained (Figure 2f and inset of Figure 2f). The effect of the increase in the ligand concentration on NP growth has been investigated by several groups, and trends of either (1) increasing[12,37,39,40] or (2) decreasing[14,19,38,41] size have been observed. This effect can be the opposite of whether it affects the nucleation or growth step. In the first case, an increase in ligand concentration tended to induce higher stabilization of the iron complex. This stabilization slows the nucleation step, which in turn lowers the number of nuclei, leading to a larger NP size. In the second case, excess ligands tend to inhibit NP growth by covering the growth sites, resulting in a smaller NP size. The

intricate interplay between the ligand concentration and the other reaction parameters (the nature and concentration of the reactants, solvent, heating rate, and reflux time), which differ from one study to another, likely explains the two opposite trends reported in the literature. In our case, the decrease in the C12-NP size from 7.8 nm to 3.2 nm with increasing the dodecanoic ligand from 1.6 mmol to 2.8 mmol, other things being equal, can be explained by the blocking of the NP growth of the growing NPs.

3.2.3. Size control of octanoic acid (C8)-coated maghemite nanoparticles

Starting again from the synthesis conditions established for the larger C18-NP size and replacing the iron oleate precursor with an iron octanoate precursor, we obtained highly polydispersed NPs (15 %) with a mean diameter of 20 nm. To obtain the desired NP population, the nature of the solvent, the ligand/precursor ratio, and the reflux time were optimized as follows: the precursor concentration was 1.6 mmol, the ratio, R, was 0.8, and the synthesis occurred in hexadecene (b.p.). 274 °C), with a reflux time of 90 min (Table 1). As shown in the TEM image and size histogram (Figure 2 g and inset of Figure 2 g), the resulting C8-NPs were characterized by mean size and size polydispersity of 11.2 nm and 13.7 %, respectively.

Decreasing the reflux time from 90 to 60 min, other things being equal, the mean size decreases from 11.2 nm to 7.0 nm keeping almost unchanged the size polydispersity, 13.4 % (Figure 2h and inset of Figure 2h). This behavior observed under our conditions, that is, with an iron octanoate precursor and hexadecene as a solvent, illustrates the time dependence of the growth process during the reflux performed at 274 °C, which corresponds to the growth temperature according to the DSC study (Figure 1c).

The smallest C8-NPs were obtained by combining the reflux time, the R-value, and the precursor concentration effects. Hence, by decreasing both the reflux time from 60 min to 30 min, the R-value from 0.8 to 0.5, and by increasing the octanoic acid concentration from 1.6 mmol to 3.2 mmol, C8-NPs with a mean diameter and size polydispersity of 3.2 nm and 12.3% respectively have been obtained (Figure 2i and insert of Figure 2i).

It is noteworthy that whatever the size is, the C8-NPs have a higher polydispersity compared to their C18- and C12-counterparts. This behavior may be explained by a more complex dissociation process of the iron octanoic precursor revealed by three endothermic events (instead of two for the C18 and C12 precursors) which are, furthermore, close to each other.

After detailing the synthesis conditions and three nanoparticle sizes obtained from each precursor, it is worth considering another intriguing parameter: saturation of the ligands used. In our study, both unsaturated oleate (C_{18}) and saturated dodecanoate (C_{12}) and octanoate (C_8) ligands were employed, introducing differences not only in chain length but also in ligand saturation. When the precursor is switched from unsaturated oleate (C_{18}) to saturated dodecanoate (C_{12}) or saturated octanoate (C_8) ligands, two key parameters are altered: chain length and ligand saturation. In addition, other experimental conditions, including the precursor ratio, solvent boiling point, and reflux time, were also modified. Therefore, isolating the specific effects of ligand unsaturation is challenging because of these simultaneous changes.

However, the Literature indicates that unsaturation in ligands such as oleate introduces a bend in the alkyl chain, leading to less ordered ligand shells compared to the more linear and ordered shells formed by saturated ligands[42–44]. This bend disrupts the tight packing, allowing for better solvent intercalation and enhanced colloidal stability. As a result, unsaturated ligands can influence the solubility of nanoparticles by facilitating better interactions with the solvent. In our study, regardless of the degree of saturation of the ligand, no significant changes in colloidal stability were observed, which remained consistently high.

These differences in solvent-ligand interactions due to ligand saturation also affect the growth mechanism of the nanoparticles. The enhanced solvent-ligand interactions, specifically the increased solubility of the ligand, led to a reduction in ligand-ligand attractions within the ligand layer surrounding the nanoparticles during their growth. This reduction weakened the integrity of the ligand layer, thereby promoting particle growth[45].

3.3. X-ray diffraction study

Figure 3 presents the X-ray diffraction (XRD) patterns for nine iron oxide nanoparticle (NP) samples, with reference patterns for maghemite (γ-Fe_2O_3) and magnetite (Fe_3O_4) employed for comparative analysis. The reference patterns correspond to maghemite (ICDD PDF card no. 04-021-3968) with a unit cell parameter of 8.336 Å and magnetite (ICDD PDF card no. 00-019-0629) with a unit cell parameter of 8.396 Å. The XRD patterns of the C12-coated NPs exhibit additional peaks attributable to dodecanoic acid. Peak broadening was observed as the nanoparticle size decreased, which is consistent with the Scherrer equation. Indexation of all samples, varying in size (7 nm and 12 nm) and surface chemistry (C18, C12, and C8), indicated a predominant alignment with maghemite rather than magnetite. Given the close similarity of the XRD patterns for these two crystalline phases, the unit cell parameters were determined by analyzing the position and broadening of the (311) reflection within the spinel structure following established procedures[46]. The unit cell parameter values for the samples summarized in Table 2 ranged from 8.334 to 8.346 nm, which closely matched the known lattice parameter of maghemite (γ-Fe_2O_3), typically approximately 8.33 nm. In contrast, magnetite (Fe_3O_4) has a slightly larger lattice parameter, approximately 8.396 nm. The calculated cell parameter values for these samples (C18-NPs, C12-NPs, and C8-NPs) suggested that the crystal phase present in these nanoparticles was predominantly maghemite rather than magnetite. This conclusion aligns with the characteristic slight reduction in the lattice parameter expected for maghemite, likely due to the presence of vacancies in the iron sites compared with the fully occupied iron sites in magnetite.

Table 2. TEM and XRD Size Analysis and Unit Cell Measurements of Iron Oxide Nanoparticles Using the (311) Plane Position and Broadening.

	TEM size (nm)	XRD size (nm)	Cell parameter (nm)
C18-NPs	12.6	6	8.345
	7.8	4.6	8.346
C12-NPs	13.3	5.1	8.335
	7.8	4.7	8.334
C8-NPs	11.2	6.8	8.336
	7	5	8.346

For the smallest nanoparticles (3 nm), The XRD peaks become larger for the smaller C18-NPs and C12-NPs, which is in line with the Scherrer equation[12,47] but the low crystallinity and significant noise in the patterns precluded a clear distinction between maghemite and magnetite, preventing the calculation of the unit cell parameters. Further analysis of the XRD pattern for the 3 nm C8-coated nanoparticles revealed more pronounced peak broadening and shifts in peak positions compared to the C18- and C12-coated samples. These shifts and broadening indicate that the diffraction patterns of the C8-coated nanoparticles may be influenced by factors other than crystallinity, such as interactions with free carboxylates or iron complexes. Consequently, the XRD pattern may not provide a straightforward interpretation of the composition. Although XRD analysis predominantly identifies maghemite as the main phase, it is important to note that the negligible presence of magnetite cannot be conclusively ruled out. The precision of XRD in distinguishing and quantifying minor phases is limited because of the similar diffraction patterns of maghemite and magnetite.

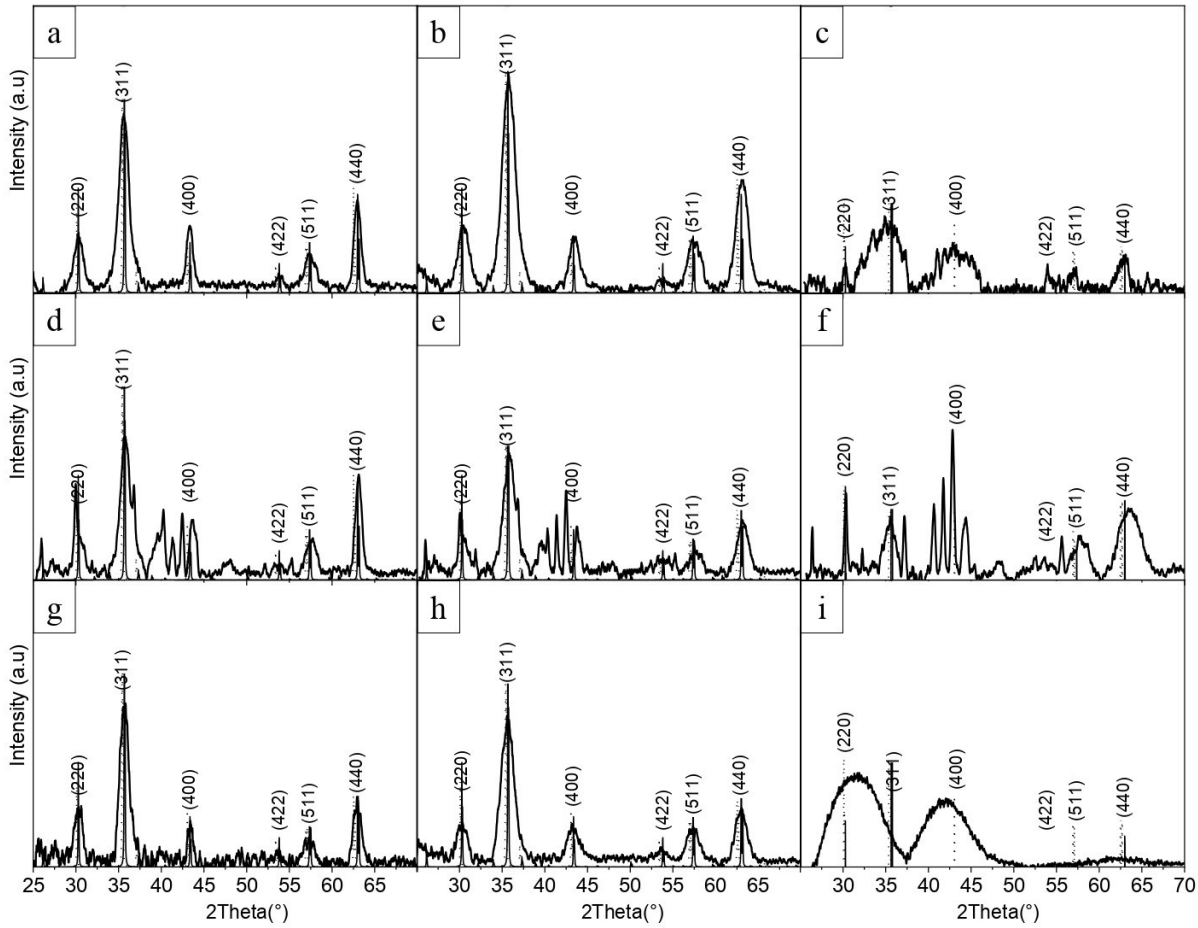

Figure 3. X-ray diffraction (XRD) patterns of iron oxide nanoparticles synthesized from (a,b,c) iron oleate, (d,e,f) iron dodeconoate, and (g,h,i) iron octanoate. The mean diameters are centered on (a,d,g) 12.0 nm, (b,e,g) 7.5 nm and (c,f,i) 3.3 nm. Solid lines: maghemite *(Ref. 04-021-3968, PDF-5)* reference pattern. Dotted lines: magnetite *(Ref. 04-027-0607, PDF-5)* reference patterns.

3.4. Magnetic properties of maghemite nanoparticles with tunable size and surface chemistry

3.4.1. Magnetization versus temperature measurements

Figure 4 shows the field-cooled (FC) and zero-field-cooled (ZFC) magnetization versus temperature curves for the nine populations of maghemite NPs presented in Figure 2, differing by both their size and surface chemistry. As the sample has been cooled in zero field, there is no net alignment of the spins at 3 K; hence, the magnetization is close to zero. A small magnetic field (1.59×10^3 Am^{-1}) was applied. As the temperature is increases, the spins become progressively "unblocked", aligning towards the field direction, and the magnetization increases until it reaches a maximum at a temperature T_{max} related to the blocking temperature T_B. Above T_B the behavior is paramagnetic i.e. the thermal energy increases to such an extent that the increased dynamic rotation of the spins prevents alignment in the field direction and the magnetization decreases with increasing temperature. In a monodisperse assembly, T_B is typically defined using equation (1):

$$T_B = KV/[k_B \ln(\tau_x/\tau_0)] \qquad (1)$$

where K, V, and k_B are the energy anisotropy constant, particle volume, and Boltzmann's constant. τ_0 is a characteristic relaxation time of 10^{-10} s for ferro- or ferrimagnetic materials and τ_x = 60 s is the experimental time scale of the susceptibility measurement. When the size polydispersity cannot be neglected, T_{max} does not coincide with T_B, as has already been discussed in refs[48–51] and the distribution

of T_B must be related to the distribution of particle volumes. The derivative $d(M_{ZFC} - M_{FC})/dT$ can be seen as the T_B distribution presenting two characteristic temperatures, namely T_{IP} for the inflection point, defined as the maximum value of $d(M_{ZFC})/dT$ (and equivalently of $d(M_{ZFC}- M_{FC})/dT$), and T_{max} where $d(M_{ZFC})/dT = 0$. Clearly, T_{IP} and T_{max} are the lower and upper bounds, respectively, of the blocking temperature corresponding to the characteristic value, $V_{0,}$ of the volume log-normal distribution, as introduced by Sappey[48] (see Table 3). For the smallest particles, <V> c.a. 3.3 nm, such a distinction is much less meaningful because of the increasing influence of spin canting and crystalline defects, making the models used for the introduction of ZFC/FC magnetizations inaccurate. Hence, in this case, we consider T_{max} as the temperature at which the entire distribution reaches the superparamagnetic regime as a more representative one.

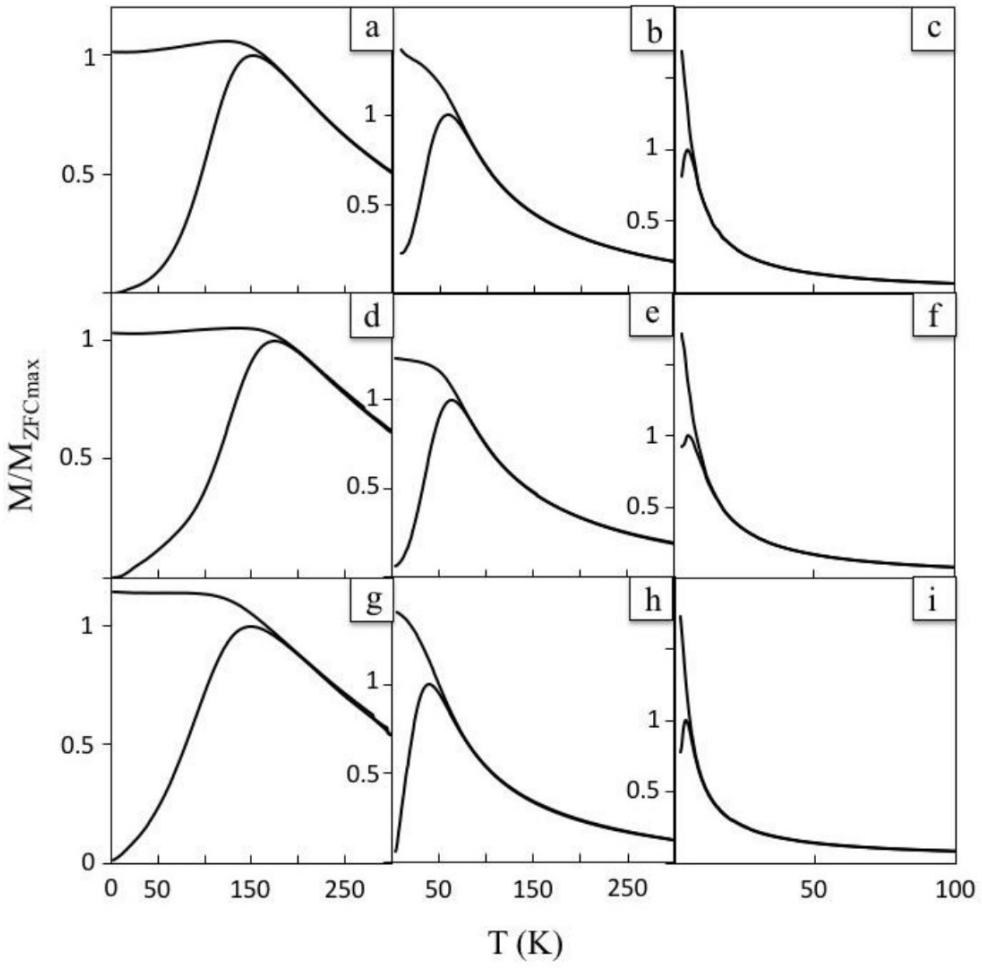

Figure 4. FC and ZFC magnetization versus temperature curves with applied field H = 1.59 x 10^3 Am^{-1}, of maghemite nanoparticles synthesized from (a,b,c) iron oleate, (d,e,f) iron dodeconoate and (g,h,i) iron octanoate. The mean diameters are centered on (a,d,g) 12.0 nm, (b,e,g) 7.5 nm and (c,f, i) 3.3 nm.

Table 3.
Magnetic parameters extracted from the ZFC magnetization and the hysteresis curves for the nine populations of maghemite nanoparticles, passivated with oleate (C18), dodecanoate (C12), and octanoate (C8) ligands. T_B: blocking temperature, M_r/M_{Hmax}: ratio of remanent-to-magnetization at Hmax (Hmax = 3.98 x 10^6 Am^{-1}), Hc: coercive field.

	Diameter (nm)	**T_B(K)**	**M_r/M_{Hmx}**	**$H_c(10^4\ Am^{-1})$**
C18-NPs	12.6 (σ = 4.0 %)	117	0.44	4.18
	7.8 (σ = 4.0 %)	45	0.38	4.02
	3.4 (σ = 14.3 %)	5	0.06	0.99
C12-NPs	13.3 (σ = 5.7 %)	124	0.34	3.34
	7.8 (σ = 6.7 %)	42	0.38	3.70
	3.2 (σ = 14.5 %)	5	0.11	0.44
C8-NPs	11.2 (σ = 13.7 %)	83	0.37	4.02
	7.0 (σ = 13.4 %)	22	0.29	2.11
	3.2 (σ = 12.3 %)	4	0.03	0.48

The larger oleic acid (C18)-coated maghemite NPs (12.6 nm) were characterized by a $T_B(v_0)$ of 117 K (Table 3). This value is in good agreement with the values reported in the literature for similar-sized C18-coated maghemite NPs[11,14]. The C12-NPs (13.3 nm) and C8-NPs (11.2 nm) were characterized by a $T_B(v_0)$ of 124 K and 83 K, respectively, similar to that of C18-NPs with sizes of the same order. For the series of larger NP_S, it is noticeable that the higher the mean diameter, the higher the T_B, which is consistent with an increase in the particle volume (See equation (1)). This magnetic trend is further illustrated for intermediate-sized NP (Table 3). Whatever the ligand is, they are characterized by a lower T_B compared to the larger NPs. The C18-NPs (7.8 nm), C12-NPs (7.8 nm), and C8-NPs (7.0 nm) were characterized by $T_B(v_0)$ values of of 45 K, 42 K, and 22 K, respectively. By focusing on the smaller NPs with a diameter of approximately 3.3 nm, T_B values were found around 5 K (Table 3). This low value of T_B is explained by their very small volume but not only. Indeed, it is likely that the spin canting, which is all the more important as the particle size is small, significantly contributes to lowering the blocking temperature. The ZFC curves for the series of larger and intermediate-sized NPs passivated with C18, C12, and C8 ligands, normalized to $T_{max,}$ are presented in (Figure 5). Whatever the NP size is, it appears that the curve for the C8-NPs is broadened concerning the ones of the C18 and C12 NPs. This reflects a larger distribution of the magnetic anisotropy energy due to a larger size distribution for the C8-NPs compared to the C12- and C18-NPs (Table 1).

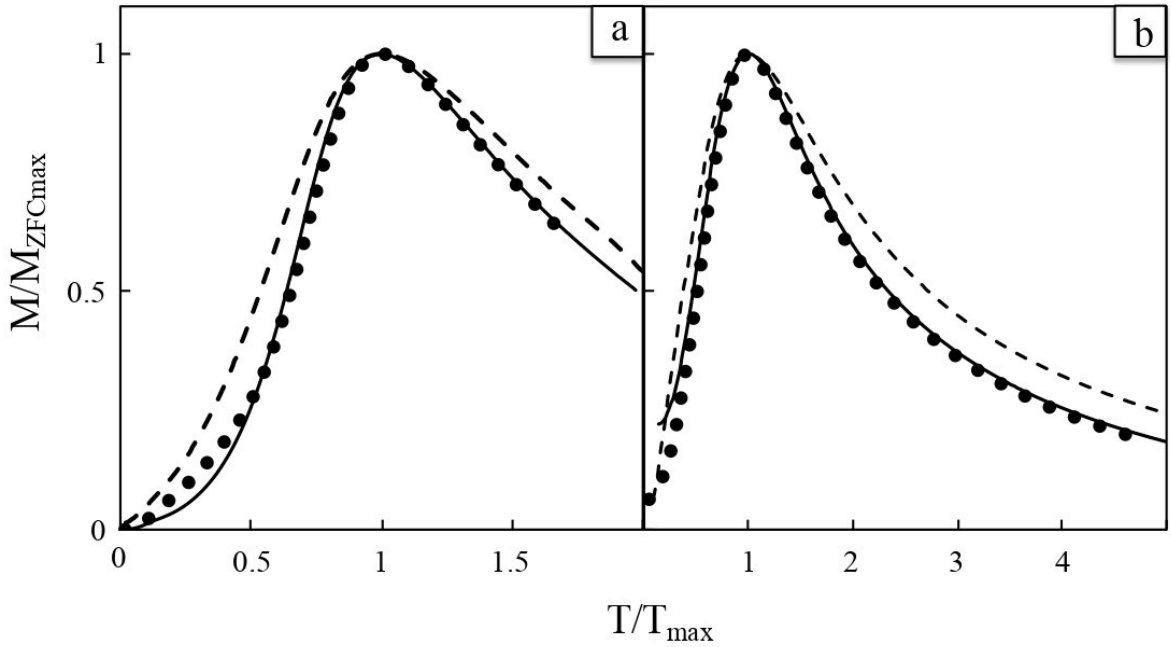

Figure 5. Zero field magnetization versus temperature curves normalized to T_{max} of maghemite nanoparticles synthesized from iron oleate (solid line), iron dodeconoate (full circles), and iron octanoate (dashed line). (a) large-nanoparticle sizes, (b) intermediate-nanoparticle sizes.

In the FC curves, the magnetization is larger than those of the ZFC curves from 3 K to T_B. Above T_B, the magnetization decreases with increasing temperature and joins the ZFC curve.
The FC curves obtained for the series of the large-size NPs (Figure 4a,d,g) show a rather flat FC curve at a temperature below T_B, which is indicative of strong dipolar interactions. However, for the intermediate- and small-sized (C18, C12, and C8) NPs (Figure 4b,c,e,f,h, i), the FC curves show an almost uniform decay before joining the ZFC curve above T_B, which suggests that the dipolar interaction effect for these samples is not predominant[52]. The stronger interactions between the larger maghemite NPs compared to the intermediate and small-size NPs can be explained in two ways. First, the washing of the larger particles, at the end of the synthesis, was more efficient compared to the intermediate- and small-size particles, ensuring a very low amount of by-products (e.g., an excess of surfactant) in the colloidal solution and then a decrease in the interparticle distance for the larger particles compared to the intermediate- and small-size NPs. Second, it is well established that dipolar interactions in the assembly of NPs increase with their volume of the NPs[53].

3.4.2. Magnetic Hysteresis Measurements

Figure 6 shows the corresponding hysteresis curves for the nine populations of maghemite NPs differing by both their size and surface chemistry. Regardless of the sample, saturation magnetization is never attained with a field H_{max} of 3.98 10^6 Am^{-1}. The magnetization curves for the larger NPs and the intermediate-sized NPs are close to saturation, while the smallest particles, owing to the more important spin canting effect and crystalline defects, likely saturate at much higher fields. The ratio of remanent-to-magnetization at H_{max} (M_r/M_{Hmax}) and the coercive field (H_c) are listed in Table 3. For the larger NPs as well as for the intermediate-size NPs, the (M_r/M_{Hmax}) is found to be approximately 0.4, which is close to the value of 0.5, expected for uniaxial anisotropy[54].

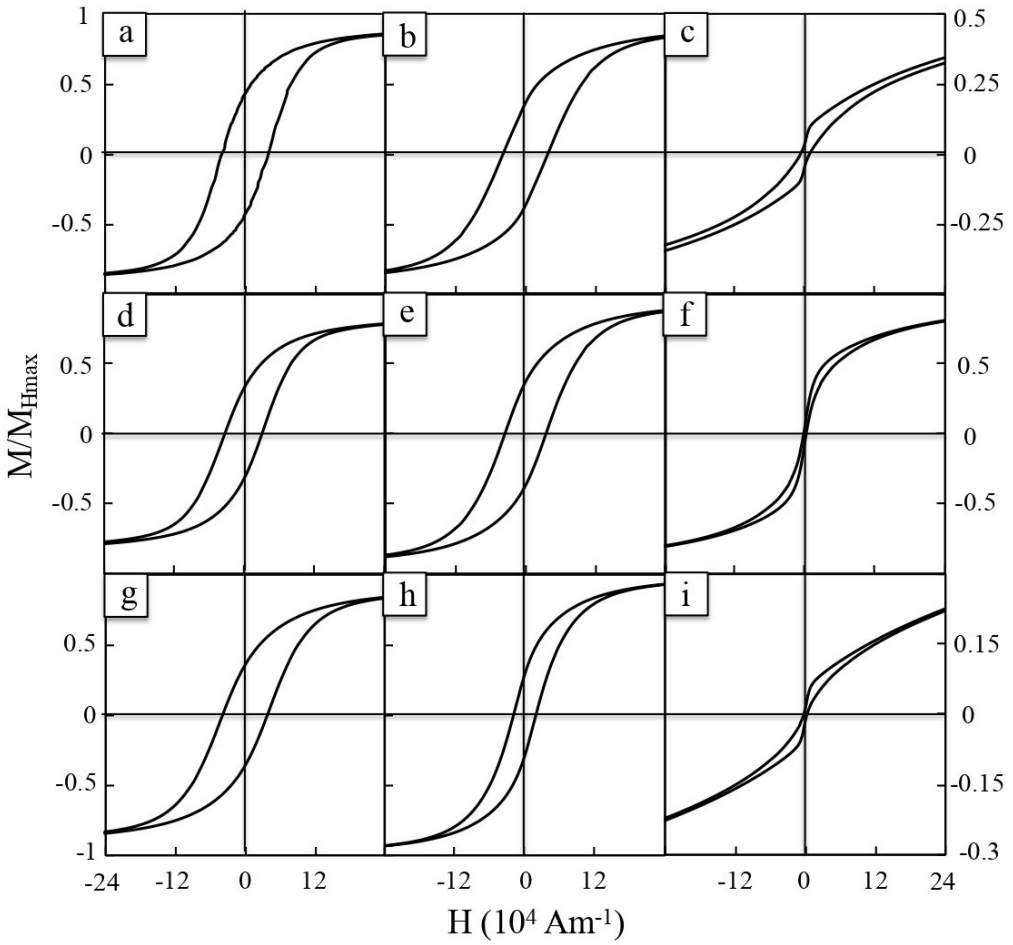

Figure 6. Hysteresis curves performed at 3 K, of maghemite nanoparticles synthesized from (a,b,c) iron oleate, (d,e,h) iron dodeconoate, and (g,h,i) iron octanoate. The mean diameters are centered on (a,d,g) 12.0 nm, (b,e,g) 7.5 nm and (c,f, i) 3.3 nm.

This magnetic behavior is in good agreement with previously reported studies[12,14,55]. However, regardless of the ligand coating, the smaller particles are characterized by a very low value (M_r/M_{Hmax}) between 0.03 and 0.11. This behavior is attributed to the fact that the measurement temperature (3K) is very close to their blocking temperature, around 5 K, i.e., a majority of the NPs display a superparamagnetic behavior. Moreover due to the small NP size, one expects that the spin canting will take a much more relative importance than in the case of the larger NPs. In a first approximation, both consequences of the small NP size, namely the small deviation between the measuring and blocking temperatures and the relative importance of the spin canting, can be modeled by adding to the distribution of NPs a component of non-anisotropic NP (K_{eff} = 0) representing either an ultra-soft phase due to the spin canting or the distribution of the smallest NPs, which are in the superparamagnetic regime (T < Tb). As a qualitative example, we performed Monte Carlo simulations (see Figure 7) of the hysteresis loop with either a single Stoner-Wolfarth component or a mixture including a non-anisotropic component. Doing this, on the one hand, one gets a reduction of both Mr/Ms and Hc and on the other hand, the shape of the hysteresis curves of the C8 and C18 samples can be qualitatively reproduced. This means that we can interpret both the sharp reduction of Hc and the shoulder of the M(h) curves for the C8 and C18 systems as a signature of the magnetic multiphase character of the corresponding NP assemblies. A similar interpretation was proposed for the behavior of the hysteresis curves of CoPt NP during annealing[56,57].

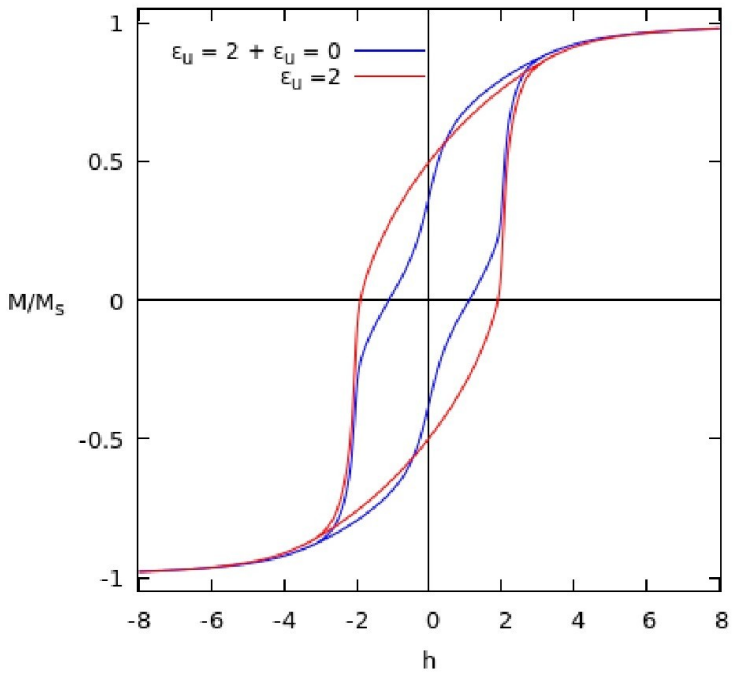

Figure 7. Monte Carlo simulation of the hysteresis curve of a single Stoner-Wolfarth model with reduced uniaxial anisotropy $e_u = 2$ and mixture including a non-anisotropic component ($\varepsilon_u = 0$). This model is given only for a qualitative purpose as the value chosen for the reduced anisotropy energy ($\varepsilon_u = 2$) is not fitted to the experimental samples. The reduced field h is H/H_r where H_r is the reference field $H_r = H_k/(2\varepsilon_u)$ and H_k the usual anisotropy field ($2K/(\mu_0 Ms)$).

CONCLUSION

In this paper, we report the first example of low-size polydisperse spherical maghemite NPs synthesized by the thermal decomposition of iron precursor with accurate control of both surface chemistry and diameter. The surface chemistry has been controlled by using three types of iron complexes, i.e., iron oleate (C18), iron dodecanoate (C12), and iron octanoate (C8) associated with the fatty acid ligands having the same alkyl chain length i.e., oleic acid (C18), dodecanoic acid (C12) and octanoic acid (C8). The optimal conditions favoring the growth of diameters centered at 3.3 nm, 7.5 nm, and 12.0 nm, for the three types of ligands, have been established. It is worth noticing that these conditions depend on the precursor length and its thermal decomposition behavior. Magnetic properties performed by SQUID magnetometry of the nine populations of maghemite NPs reflect the accurate size control. A potential future direction for research in this field is to study the impact of the ligands differing by their chemical nature and chain length on the NP interactions with their environment (solvent, polymer, … etc). Controlling the ligand chain length of the maghemite NPs organized in supercrystals is of great importance to tune the structural characteristics of these nanomaterials, i.e., the interparticle distance and the 3D crystalline structure. Such magnetic superlattices provide a new horizon in fundamental physics and can be used as model systems for considering phenomena related to dipolar interactions within the solid and in particular the dipolar superferromagnetism (SFM), expected in highly dense supercrystals.

ACKNOWLEDGEMENTS:
The authors thank the ANR NanoHype « Temperature Profile in Nanomagnet-based Hyperthermia Devices» (contract number ANR-21-CE09-0043) and the LEEGO chair program for supporting this work. S.M. gratefully acknowledges the financial support from the Materials Institute for the Ph.D. Scholarship, contract number IMAT – DOCTORANT SORBR122RRO. Additionally, the Authors thank François Oudet, Caroline Lefebvre, and Frédéric Nadaud from the Physico-Chemical Analysis Service (SAPC) for their contributions.

REFERENCES

(1) Sheng, S.; Liu, W.; Zhu, K.; Cheng, K.; Ye, K.; Wang, G.; Cao, D.; Yan, J. Fe3O4 Nanospheres in Situ Decorated Graphene as High-Performance Anode for Asymmetric Supercapacitor with Impressive Energy Density. *J. Colloid Interface Sci.* 2019, *536*, 235–244. https://doi.org/10.1016/j.jcis.2018.10.060.
(2) Rajabi, F.; Pineda, A.; Naserian, S.; Balu, A. M.; Luque, R.; Romero, A. A. Aqueous Oxidation of Alcohols Catalysed by Recoverable Iron Oxide Nanoparticles Supported on Aluminosilicates. *Green Chem.* 2013, *15* (5), 1232. https://doi.org/10.1039/c3gc40110c.
(3) Nguyen, M. D.; Tran, H.-V.; Xu, S.; Lee, T. R. Fe3O4 Nanoparticles: Structures, Synthesis, Magnetic Properties, Surface Functionalization, and Emerging Applications. *Appl. Sci.* 2021, *11* (23), 11301. https://doi.org/10.3390/app112311301.
(4) Andrade, R. G. D.; Veloso, S. R. S.; Castanheira, E. M. S. Shape Anisotropic Iron Oxide-Based Magnetic Nanoparticles: Synthesis and Biomedical Applications. *Int. J. Mol. Sci.* 2020, *21* (7), 2455. https://doi.org/10.3390/ijms21072455.
(5) Rebodos, R. L.; Vikesland, P. J. Effects of Oxidation on the Magnetization of Nanoparticulate Magnetite. *Langmuir* 2010, *26* (22), 16745–16753. https://doi.org/10.1021/la102461z.
(6) Shokrollahi, H. A Review of the Magnetic Properties, Synthesis Methods and Applications of Maghemite. *J. Magn. Magn. Mater.* 2017, *426*, 74–81. https://doi.org/10.1016/j.jmmm.2016.11.033.
(7) Ansari, S. A. M. K.; Ficiarà, E.; Ruffinatti, F. A.; Stura, I.; Argenziano, M.; Abollino, O.; Cavalli, R.; Guiot, C.; D'Agata, F. Magnetic Iron Oxide Nanoparticles: Synthesis, Characterization and Functionalization for Biomedical Applications in the Central Nervous System. *Mater. Basel Switz.* 2019, *12* (3), 465. https://doi.org/10.3390/ma12030465.
(8) Sun, S.; Zeng, H. Size-Controlled Synthesis of Magnetite Nanoparticles. *J. Am. Chem. Soc.* 2002, *124* (28), 8204–8205. https://doi.org/10.1021/ja026501x.
(9) Jana, N. R.; Chen, Y.; Peng, X. Size- and Shape-Controlled Magnetic (Cr, Mn, Fe, Co, Ni) Oxide Nanocrystals via a Simple and General Approach. *Chem. Mater.* 2004, *16* (20), 3931–3935. https://doi.org/10.1021/cm049221k.
(10) Redl, F. X.; Black, C. T.; Papaefthymiou, G. C.; Sandstrom, R. L.; Yin, M.; Zeng, H.; Murray, C. B.; O'Brien, S. P. Magnetic, Electronic, and Structural Characterization of Nonstoichiometric Iron Oxides at the Nanoscale. *J. Am. Chem. Soc.* 2004, *126* (44), 14583–14599. https://doi.org/10.1021/ja046808r.
(11) Park, J.; An, K.; Hwang, Y.; Park, J.-G.; Noh, H.-J.; Kim, J.-Y.; Park, J.-H.; Hwang, N.-M.; Hyeon, T. Ultra-Large-Scale Syntheses of Monodisperse Nanocrystals. *Nat. Mater.* 2004, *3* (12), 891–895. https://doi.org/10.1038/nmat1251.
(12) Demortière, A.; Panissod, P.; Pichon, B. P.; Pourroy, G.; Guillon, D.; Donnio, B.; Bégin-Colin, S. Size-Dependent Properties of Magnetic Iron Oxide Nanocrystals. *Nanoscale* 2011, *3* (1), 225–232. https://doi.org/10.1039/C0NR00521E.
(13) Pauly, M.; Pichon, B. P.; Panissod, P.; Fleutot, S.; Rodriguez, P.; Drillon, M.; Begin-Colin, S. Size Dependent Dipolar Interactions in Iron Oxide Nanoparticle Monolayer and Multilayer Langmuir–Blodgett Films. *J. Mater. Chem.* 2012, *22* (13), 6343–6350. https://doi.org/10.1039/C2JM15797G.
(14) Baaziz, W.; Pichon, B. P.; Fleutot, S.; Liu, Y.; Lefevre, C.; Greneche, J.-M.; Toumi, M.; Mhiri, T.; Begin-Colin, S. Magnetic Iron Oxide Nanoparticles: Reproducible Tuning of the Size and Nanosized-Dependent Composition, Defects, and Spin Canting. *J. Phys. Chem. C* 2014, *118* (7), 3795–3810. https://doi.org/10.1021/jp411481p.
(15) Baaziz, W.; Pichon, B. P.; Grenèche, J.-M.; Begin-Colin, S. Effect of Reaction Environment and in Situ Formation of the Precursor on the Composition and Shape of Iron Oxide Nanoparticles

Synthesized by the Thermal Decomposition Method. *CrystEngComm* 2018, *20* (44), 7206–7220. https://doi.org/10.1039/C8CE00875B.
(16) Kovalenko, M. V.; Bodnarchuk, M. I.; Lechner, R. T.; Hesser, G.; Schäffler, F.; Heiss, W. Fatty Acid Salts as Stabilizers in Size- and Shape-Controlled Nanocrystal Synthesis: The Case of Inverse Spinel Iron Oxide. *J. Am. Chem. Soc.* 2007, *129* (20), 6352–6353. https://doi.org/10.1021/ja0692478.
(17) Yang, H.; Ogawa, T.; Hasegawa, D.; Takahashi, M. Synthesis and Magnetic Properties of Monodisperse Magnetite Nanocubes. *J. Appl. Phys.* 2008, *103* (7), 07D526. https://doi.org/10.1063/1.2833820.
(18) Kim, D.; Lee, N.; Park, M.; Kim, B. H.; An, K.; Hyeon, T. Synthesis of Uniform Ferrimagnetic Magnetite Nanocubes. *J. Am. Chem. Soc.* 2009, *131* (2), 454–455. https://doi.org/10.1021/ja8086906.
(19) Guardia, P.; Pérez, N.; Labarta, A.; Batlle, X. Controlled Synthesis of Iron Oxide Nanoparticles over a Wide Size Range. *Langmuir* 2010, *26* (8), 5843–5847. https://doi.org/10.1021/la903767e.
(20) Pauly, M.; Pichon, B. P.; Albouy, P.-A.; Fleutot, S.; Leuvrey, C.; Trassin, M.; Gallani, J.-L.; Begin-Colin, S. Monolayer and Multilayer Assemblies of Spherically and Cubic-Shaped Iron Oxide Nanoparticles. *J. Mater. Chem.* 2011, *21* (40), 16018–16027. https://doi.org/10.1039/C1JM12012C.
(21) Zhang, L.; Wu, J.; Liao, H.; Hou, Y.; Gao, S. Octahedral Fe3O4nanoparticles and Their Assembled Structures. *Chem. Commun.* 2009, No. 29, 4378–4380. https://doi.org/10.1039/B906636E.
(22) Zhao, Z.; Zhou, Z.; Bao, J.; Wang, Z.; Hu, J.; Chi, X.; Ni, K.; Wang, R.; Chen, X.; Chen, Z.; Gao, J. Octapod Iron Oxide Nanoparticles as High-Performance T2 Contrast Agents for Magnetic Resonance Imaging. *Nat. Commun.* 2013, *4* (1), 2266. https://doi.org/10.1038/ncomms3266.
(23) Zhou, Z.; Zhu, X.; Wu, D.; Chen, Q.; Huang, D.; Sun, C.; Xin, J.; Ni, K.; Gao, J. Anisotropic Shaped Iron Oxide Nanostructures: Controlled Synthesis and Proton Relaxation Shortening Effects. *Chem. Mater.* 2015, *27* (9), 3505–3515. https://doi.org/10.1021/acs.chemmater.5b00944.
(24) Roca, A. G.; Gutiérrez, L.; Gavilán, H.; Fortes Brollo, M. E.; Veintemillas-Verdaguer, S.; Morales, M. D. P. Design Strategies for Shape-Controlled Magnetic Iron Oxide Nanoparticles. *Adv. Drug Deliv. Rev.* 2019, *138*, 68–104. https://doi.org/10.1016/j.addr.2018.12.008.
(25) Park, J.; Joo, J.; Kwon, S. G.; Jang, Y.; Hyeon, T. Synthesis of Monodisperse Spherical Nanocrystals. *Angew. Chem. Int. Ed Engl.* 2007, *46* (25), 4630–4660. https://doi.org/10.1002/anie.200603148.
(26) Wu, L.; Mendoza-Garcia, A.; Li, Q.; Sun, S. Organic Phase Syntheses of Magnetic Nanoparticles and Their Applications. *Chem. Rev.* 2016, *116* (18), 10473–10512. https://doi.org/10.1021/acs.chemrev.5b00687.
(27) Meftah, S.; Ngo, A.-T.; Shahmanesh, A.; Courty, A.; Kondo, D.; Bedoui, F.; Lisiecki, I. Striking Effect of the Iron Stearate Purity on the Shape and Size of Maghemite Nanoparticles. *Colloids Surf. Physicochem. Eng. Asp.* 2024, *680*, 132689. https://doi.org/10.1016/j.colsurfa.2023.132689.
(28) Dehsari, H. S.; Ribeiro, A. H.; Ersöz, B.; Tremel, W.; Jakob, G.; Asadi, K. Effect of Precursor Concentration on Size Evolution of Iron Oxide Nanoparticles. *CrystEngComm* 2017, *19* (44), 6694–6702. https://doi.org/10.1039/C7CE01406F.
(29) Henry, A.-I.; Courty, A.; Pileni, M.-P.; Albouy, P.-A.; Israelachvili, J. Tuning of Solid Phase in Supracrystals Made of Silver Nanocrystals. *Nano Lett.* 2008, *8* (7), 2000–2005. https://doi.org/10.1021/nl8010947.
(30) Lee, S.; Ngo, A.-T.; Lisiecki, I.; Courty, A. Structural Diversity in Binary Superlattices from Au and γ-Fe2O3 Nanocrystals: Towards Fine Tuning of Dipolar Interactions. *Mater. Chem. Front.* 2022, *6* (13), 1814–1823. https://doi.org/10.1039/D2QM00139J.
(31) Wan, Y.; Goubet, N.; Albouy, P.-A.; Schaeffer, N.; Pileni, M.-P. Hierarchy in Au Nanocrystal Ordering in a Supracrystal: II. Control of Interparticle Distances. *Langmuir ACS J. Surf. Colloids* 2013, *29* (44), 13576–13581. https://doi.org/10.1021/la403583q.
(32) Wan, Y. F.; Goubet, N.; Albouy, P. A.; Pileni, M. P. Hierarchy in Au Nanocrystal Ordering in Supracrystals: A Potential Approach to Detect New Physical Properties. *Langmuir ACS J. Surf. Colloids* 2013, *29* (24), 7456–7463. https://doi.org/10.1021/la3045187.

(33) Navarro Oliva, F. S.; Sahihi, M.; Lenglet, L.; Ospina, A.; Guenin, E.; Jaramillo-Botero, A.; Goddard, W. A.; Bedoui, F. Nanoparticle Size and Surface Chemistry Effects on Mechanical and Physical Properties of Nano-Reinforced Polymers: The Case of PVDF-Fe3O4 Nano-Composites. *Polym. Test.* 2023, *117*, 107851. https://doi.org/10.1016/j.polymertesting.2022.107851.
(34) Bedoui, F.; Sahihi, M.; Jaramillo-Botero, A.; Goddard, W. A. I. Enhancing Multifunctionality: Optimal Properties of Iron-Oxide-Reinforced Polyvinylidene Difluoride Unveiled Through Full Atom Molecular Dynamics Simulations. *Langmuir* 2024, *40* (15), 8067–8073. https://doi.org/10.1021/acs.langmuir.3c04011.
(35) Bronstein, L. M.; Huang, X.; Retrum, J.; Schmucker, A.; Pink, M.; Stein, B. D.; Dragnea, B. Influence of Iron Oleate Complex Structure on Iron Oxide Nanoparticle Formation. *Chem. Mater.* 2007, *19* (15), 3624–3632. https://doi.org/10.1021/cm062948j.
(36) Balakrishnan, T.; Lee, M.-J.; Dey, J.; Choi, S.-M. Sub-Nanometer Scale Size-Control of Iron Oxide Nanoparticles with Drying Time of Iron Oleate. *CrystEngComm* 2019, *21* (27), 4063–4071. https://doi.org/10.1039/C9CE00112C.
(37) Hufschmid, R.; Arami, H.; Ferguson, R. M.; Gonzales, M.; Teeman, E.; Brush, L. N.; Browning, N. D.; Krishnan, K. M. Synthesis of Phase-Pure and Monodisperse Iron Oxide Nanoparticles by Thermal Decomposition. *Nanoscale* 2015, *7* (25), 11142–11154. https://doi.org/10.1039/c5nr01651g.
(38) Vargas, J. M.; Zysler, R. D. Tailoring the Size in Colloidal Iron Oxide Magnetic Nanoparticles. *Nanotechnology* 2005, *16* (9), 1474. https://doi.org/10.1088/0957-4484/16/9/009.
(39) W. Yu, W.; C. Falkner, J.; T. Yavuz, C.; L. Colvin, V. Synthesis of Monodisperse Iron Oxide Nanocrystals by Thermal Decomposition of Iron Carboxylate Salts. *Chem. Commun.* 2004, *0* (20), 2306–2307. https://doi.org/10.1039/B409601K.
(40) Zhu, Y.; Jiang, F. Y.; Chen, K.; Kang, F.; Tang, Z. K. Size-Controlled Synthesis of Monodisperse Superparamagnetic Iron Oxide Nanoparticles. *J. Alloys Compd.* 2011, *509* (34), 8549–8553. https://doi.org/10.1016/j.jallcom.2011.05.115.
(41) Moya, C.; Batlle, X.; Labarta, A. The Effect of Oleic Acid on the Synthesis of Fe3−xO4 Nanoparticles over a Wide Size Range. *Phys. Chem. Chem. Phys.* 2015, *17* (41), 27373–27379. https://doi.org/10.1039/C5CP03395K.
(42) Calvin, J. J.; Brewer, A. S.; Alivisatos, A. P. The Role of Organic Ligand Shell Structures in Colloidal Nanocrystal Synthesis. *Nat. Synth.* 2022, *1* (2), 127–137. https://doi.org/10.1038/s44160-022-00025-4.
(43) Tadmor, R.; Rosensweig, R. E.; Frey, J.; Klein, J. Resolving the Puzzle of Ferrofluid Dispersants. *Langmuir* 2000, *16* (24), 9117–9120. https://doi.org/10.1021/la0009137.
(44) Gupta, A. K.; Gupta, M. Synthesis and Surface Engineering of Iron Oxide Nanoparticles for Biomedical Applications. *Biomaterials* 2005, *26* (18), 3995–4021. https://doi.org/10.1016/j.biomaterials.2004.10.012.
(45) Costanzo, S.; Simon, G.; Richardi, J.; Colomban, Ph.; Lisiecki, I. Solvent Effects on Cobalt Nanocrystal Synthesis—A Facile Strategy To Control the Size of Co Nanocrystals. *J. Phys. Chem. C* 2016, *120* (38), 22054–22061. https://doi.org/10.1021/acs.jpcc.6b07293.
(46) Roca, A. G.; Marco, J. F.; Morales, M. del P.; Serna, C. J. Effect of Nature and Particle Size on Properties of Uniform Magnetite and Maghemite Nanoparticles. *J. Phys. Chem. C* 2007, *111* (50), 18577–18584. https://doi.org/10.1021/jp075133m.
(47) Patterson, A. L. The Scherrer Formula for X-Ray Particle Size Determination. *Phys. Rev.* 1939, *56* (10), 978–982. https://doi.org/10.1103/PhysRev.56.978.
(48) Sappey, R.; Vincent, E.; Hadacek, N.; Chaput, F.; Boilot, J. P.; Zins, D. Nonmonotonic Field Dependence of the Zero-Field Cooled Magnetization Peak in Some Systems of Magnetic Nanoparticles. *Phys. Rev. B* 1997, *56* (22), 14551–14559. https://doi.org/10.1103/PhysRevB.56.14551.
(49) Bruvera, I. J.; Mendoza Zélis, P.; Pilar Calatayud, M.; Goya, G. F.; Sánchez, F. H. Determination of the Blocking Temperature of Magnetic Nanoparticles: The Good, the Bad, and the Ugly. *J. Appl. Phys.* 2015, *118* (18), 184304. https://doi.org/10.1063/1.4935484.
(50) Livesey, K. L.; Ruta, S.; Anderson, N. R.; Baldomir, D.; Chantrell, R. W.; Serantes, D. Beyond the Blocking Model to Fit Nanoparticle ZFC/FC Magnetisation Curves. *Sci. Rep.* 2018, *8* (1), 11166. https://doi.org/10.1038/s41598-018-29501-8.

(51) Schmitz-Antoniak, C. X-Ray Absorption Spectroscopy on Magnetic Nanoscale Systems for Modern Applications. *Rep. Prog. Phys.* 2015, *78* (6), 062501. https://doi.org/10.1088/0034-4885/78/6/062501.
(52) Tronc, E.; Prene, P.; Jolivet, J. P.; d'Orazio, F.; Lucari, F.; Fiorani, D.; Godinho, M.; Cherkaoui, R.; Nogues, M.; Dormann, J. L. Magnetic Behaviour of γ-Fe2O3 Nanoparticles by Mössbauer Spectroscopy and Magnetic Measurements. *Hyperfine Interact.* 1995, *95* (1), 129–148. https://doi.org/10.1007/BF02146310.
(53) Kechrakos, D.; Trohidou, K. N. Magnetic Properties of Self-Assembled Interacting Nanoparticles. *Appl. Phys. Lett.* 2002, *81* (24), 4574–4576. https://doi.org/10.1063/1.1528290.
(54) Stoner, E. C.; Wohlfarth, E. P. A Mechanism of Magnetic Hysteresis in Heterogeneous Alloys. *IEEE Trans. Magn.* 1991, *27* (4), 3475–3518. https://doi.org/10.1109/TMAG.1991.1183750.
(55) Ngo, A. T.; Pileni, M. P. Assemblies of Ferrite Nanocrystals: Partial Orientation of the Easy Magnetic Axes. *J. Phys. Chem. B* 2001, *105* (1), 53–58. https://doi.org/10.1021/jp002243j.
(56) Sehdev, N.; Medwal, R.; Annapoorni, S. Enhanced Phase Stabilization of CoPt in the Presence of Ag. *J. Appl. Phys.* 2011, *110* (3), 033901. https://doi.org/10.1063/1.3615939.
(57) Kim, J. Fabrication of CoPt Nanoparticles with High Coercivity on a Polymer Film. *Colloids Surf. Physicochem. Eng. Asp.* 2007.